PNAS

Supporting Information for

Intrinsic Tensile Ductility in Strain Hardening Multi-Principal Element Metallic Glass

Zhibo Zhang[a,1], Shan Zhang [a,b,1], Qing Wang[c], Anliang Lu[a], Zhaoqi Chen[a], Ziyin Yang[a], Junhua Luan[d], Rui Su[b], Pengfei Guan[b,2], Yong Yang[a,d,2].

[a.] Department of Mechanical Engineering, College of Engineering, City University of Hong Kong, Tat Chee Avenue, Kowloon Tong, Kowloon, Hong Kong, China

[b.] Beijing Computational Science Research Center, Beijing 100193, China

[c.] Laboratory for Microstructures, Institute of Materials, Shanghai University, Shanghai, China

[d.] Department of Materials Science and Engineering, College of Engineering, City University of Hong Kong, Tat Chee Avenue, Kowloon Tong, Kowloon, Hong Kong, China.

[1.] *These authors contributed equally to this work.*

[2.] *To whom correspondence should be addressed:* Pengfei Guan and Yong Yang.

Email: pguan@csrc.ac.cn, yonyang@cityu.edu.hk

This PDF file includes:

Supporting text
Figures S1 to S21
Tables S1 to S3
Legends for Movies S1 to S3
SI References

Other supporting materials for this manuscript include the following:

Movies S1 to S3

Supporting Information Text

Here we present the implementation of neural network inter-atomic potentials (NNAP) capable of simulating the mechanical/physical behavior of the TiZrHfCo high-entropy metallic glass (MPEMG). The **Methods** section outlines the database preparation, local atomic environment interpreter (also called symmetry functions), and neural network training. To validate the NNAP, the **Properties** section benchmarks its predictions against ab-initio calculations and experimental results.

1 Methods

1.1 Database

In order to create TiZrHfCo potentials, an extensive dataset comprising elemental, binary, ternary, and quaternary configurations with diverse compositions and morphologies is essential. To accomplish this, we employed a comprehensive dataset consisting of 34,809 labeled data points (**Fig. S14**), curated to ensure a precise representation of the potential energy surface. This dataset served as the foundation for training a pre-existing model specifically defined for ternary potentials, as outlined in our recent publication (1).

1.2 Structure Descriptors

To produce a reliable NNAP, we chose an appropriate representation of atomic neighborhood environments (2, 3). To introduce the Spherical Chebyshev (SC) basis, the density function $\rho(r)$ of the local environment could be:

$$\rho(r) = \sum_{i \neq j} w(t_j)\delta(r - r_{ij})f_c(r_{ij}) \quad [1]$$

where $w(t_j)$ is a weight parameter of chemical specie t_j,

$$w(t_j) = (-1)^{t_j - 1}t_j, t_j = 1,2, \dots, n_t \quad [2]$$

$w(t_j)$ the actual weight function can be learned automatically due to additional weight parameters in the neural networks (4). $\delta(r - r_{ij})$ is Dirac's delta function, radial cutoff function. $\rho(r)$ is then expanded in the spherical coordinates:

$$c_{nlm} = \sum_{i \neq j} w(t_j)R_n(r_{ij})Y_{lm}(\theta, \varphi)f_c(r_{ij}) \quad [3]$$

$Y_{lm}(\theta, \varphi)$ is the spherical harmonic function used to describe the angular information of the atomic environment. $f_c(r_{ij})$ is a cutoff function which smoothly decays to zero at neighbor cutoff r_c, which can be expressed as:

$$f_c(r_{ij}) = \begin{cases} (1 - (\frac{r_{ij}}{r_c})^2)^4, & r_{ij} < r_c \\ 0, & r_{ij} \geq r_c \end{cases} \quad [4]$$

Here, the cutoff radius set r_c to 7 Å in this work. $R_n(r_{ij})$ the first kind $T_n(x)$ of r_{ij} Chebyshev functions after linear transformation, where a linear transform is applied to map x to $[0, r_c]$ and used to describe the radial information of the atomic environment, and it is expressed as:

$$R_n(r_{ij}) = T_n(1 - \frac{2r_{ij}}{r_c}) \quad [5]$$

However, since c_{nlm} does not have rotational invariance, a local environment real-valued descriptor satisfying rotational invariance concerning c_{nlm} was used, expressed as

$$P_{nl} = \frac{4\pi}{2l+1}\sum_{|m| \leq l} c^*_{nlm}c_{nlm} \quad [6]$$

In this work, the values of n of the Chebyshev polynomials are taken from 0 to 4, while the values of l of the spherical harmonic function are taken from 0 to 8. We chose a neural network architecture with 90 input nodes, four hidden layers of 16 nodes each, and one output node, resulting in a 90-16-16-16-16-1 network structure. The activation function is the sigmoid linear unit (SiLU) function for each neuron in the neural

network's hidden layer. The weight optimization of the neural network adopts the LBFGS-B algorithm (5), and the loss function L is expressed as:

$$L = \frac{1}{2}\sum_{N}^{samples} e_n^2 + \frac{1}{2}\sum_{l}^{weights} w_l^2 \quad [7]$$

Where the variable e_n represents the energy difference between the neural networks' predicted energy and the reference energy for each reference sample n, while w_l iterates through all the weights of the neural network. The coefficient of the penalty term in this study is set as λ = 0.005. Along with a bias, the 9156 degrees of freedom vector will serve as the neural network's input layer. The bias term helps to shift the activation function of each neuron, effectively changing the decision boundary and allowing the network to make better predictions, which serves as the input of the NNAP models.

1.3 Overall NNAP Accuracy

To evaluate how well our NNAP performs, we divided our dataset into a training set and a testing set with a ratio of 9:1, randomly and with the same distribution of formation energy. We used the divergence of root-mean-square error (RMSE) between the training and testing sets to indicate overfitting, which helped us implement early stopping strategies. In the final iteration, the RMSE of the testing set in the final iteration reached 9.07 meV/atom, which was generally acceptable in MD simulations of quaternary compounds (**Fig. S15**).

1.4 Equation of States Validation

We utilized ab-initio calculations in constructing NNAP and fit the curve of energy versus volume for various ordered binary compounds (**Fig. S16**) with the Murnaghan equation of states (6) (EOS).

2 Properties

2.1 Thermodynamic property

The τ_α, representing the relaxation dynamics, which is usually defined as the time until the $F_s(q,t)$ (7) decays to 1/e, are plotted in **Fig. S18(a)**

$$F_s(q,t) = \frac{1}{N}\langle\sum_{l=1}^{N} exp\{-i\vec{q}\cdot[\vec{r}_l(t) - \vec{r}_l(0)]\}\rangle \quad [8]$$

where N is the number of the systems, q is the wave vector, and $\vec{r}_l(t) - \vec{r}_l(0)$ represents the displacement vector of atom l over a given time interval t, < > denotes the ensemble average over different configurations. The VFT (Volger-Fulcher-Tammann) function (8) $\tau = \tau_0 \cdot e^{\frac{BT_0}{T-T_0}}$ was employed to fit the data (**Fig. S18(b)**), where τ_0, B, and T_0 are fitting parameters and empirical material-dependent. The glass transition temperature (9), T_g, is defined as τ (T=T_g) = 10^4 ps. We defined the kinetic fragility index (10) in MD simulation, m, as the slope of the τ_α curves at T_g by $m = \left.\frac{d\log\tau}{dT_g/T}\right|_{T_g}$ (**Fig. S18(c)**) (11). Finally, m of the 8000-atom $Ti_{25}Zr_{25}Hf_{25}Co_{25}$ MPEMG was 152.

2.2 Activation Energy of Beta Relaxation

We employed the CG algorithm to prepare the inherent structure of 2000-atom MPEMGs with Co concentrations of 6%, 10%, 25%, and 40%, quenched from 2000K to 300K at a rate of 10^{13}K/s. Once the sample reached 300K, the system was allowed to relax for 1 ns using the Isothermal–isobaric (NPT) ensemble. We applied 3 activation-relaxation technique (ART) (12) searches for each atom. We randomly set the initial perturbation displacement of 0.5 Å and the direction of perturbation in the searching events. The perturbation radius is 3.8 Å. And the force threshold is below 0.05 eV/Å. Thus, we could get the raw data by 6,000 ART events for a given sample. We should use two removal steps (13) to obtain ~ 3,500 effective searches (in different samples, the number will be different). Finally, we can get the activation energy spectrum for each sample in Fig. S8a.

The arithmetic mean of E_A ($\overline{E}_{A,k}$), and Effective barrier $\overline{E}_A$

Eq. [9] (14) calculated the effective barrier of fast beta relaxation to keep low energy barriers dominating the diffusivity.

$$\bar{E}_A(E_{IS},T) = -K_B T \cdot ln\left[\int P(E_A|E_{IS})\mathrm{e}^{-\frac{E_A}{k_B T}}\,\mathrm{d}E_A\right] \quad [9]$$

We used the arithmetic mean of each atom's E_A, $\bar{E}_{A,k}$, (15) to describe the activation energy of the secondary relaxation process. It was calculated by Eq. [10]

$$\bar{E}_{A,k} = \frac{1}{N_{event,k}}\sum_{i=1}^{N_{event,k}} E_A(i,k) \quad [10]$$

where $E_A(i,k)$ is the k atom's activation energy in the ith event. $N_{event,k}$ is the number of the effective events of the k atom.

2.3 MD simulation of shear

$$\bar{q}_l(i) = \left(\frac{4\pi}{2l+1}\sum_{m=-l}^{l}\frac{1}{\tilde{N}(i)}\sum_{k=0}^{\tilde{N}(i)} q_{lm}(k)^2\right)^{\frac{1}{2}} \quad [11]$$

where:

$$q_{lm}(k) = \frac{1}{N(k)}\sum_{j=1}^{N(k)}\frac{A_{kj}}{A}Y_{lm}(r_{kj}) \quad [12]$$

Here, the sum from k=0 to $\tilde{N}(i)$ runs over all neighbors of particle i plus the particle i itself. Thus, to calculate $\bar{q}_l(i)$ of particle i one uses the local orientational order vectors $q_{lm}(i)$ averaged over particle i and its surroundings (16, 17). While $q_l(i)$ holds the information of the structure of the first shell around particle i, its averaged $\bar{q}_l(i)$ version also considers the second shell. Here, $N(k)$ is the number of nearest neighbors of particle i, l is a free integer parameter, and m is an integer that runs from $m=-l$ to $m=+l$. The functions Y_{lm} are the spherical harmonics and r_{kj} is the vector from particle k to particle j. A_{kj} is the surface area of the Voronoi cell facet. A is the sum of the areas of the Voronoi faces of the atom k.

2.4 Energy of Crystal with Different Compositions

The structure of HCP crystals of different components is optimized by using DFT to obtain their configuration, energy, and composition relationship. The content of Hf remained almost the same, Zr increased, Ti, and Co decreased. Fig. S20 shows the potential energies of the HCP crystals with the varying compositions of Ti and Co.

2.5 Enthalpy of Mixing with Different Compositions

NNP-MD simulations to calculate the enthalpy of mixing between Co and TiZrHf in the $Co_x(TiZrHf)_{1-x}$ system using the ML potential. We prepared 1000-atom glass samples with different Co concentration, ranging from 5% to 40% and prepared 1000-atom crystal samples of Co and TiZrHf. The sample was cooled down from 2400K to 300K at a rate of 10^{14} K/s. Once the sample reached 300K, the system was allowed to relax for 2 ns using the Isothermal–isobaric (NPT) ensemble. We followed a well-established approach in the literature (18) to ensure the validity of our results.

$$\Delta H_m \approx \Delta E_p = E_{Co_x TiHfZr_{(1-x)}} - \mathrm{x} * E^0_{Co} - (1-\mathrm{x}) * E^0_{TiHfZr} \quad [13]$$

Where E^0_{Co} *and* E^0_{TiHfZr} were the crystal potential energy. $E_{Co_x TiHfZr_{(1-x)}}$ was the relaxed amorphous potential energy of $Co_x(TiZrHf)_{1-x}$, and x was the Co's content. Fig. S21 shows the enthalpy of mixing between Co and TiZrHf in the $Co_x(TiZrHf)_{1-x}$ system. We found that at 300K, the enthalpy of mixing

increases with the decreasing concentration of Co, and suggests a tendency for Co segregation in the Co-lean regions.

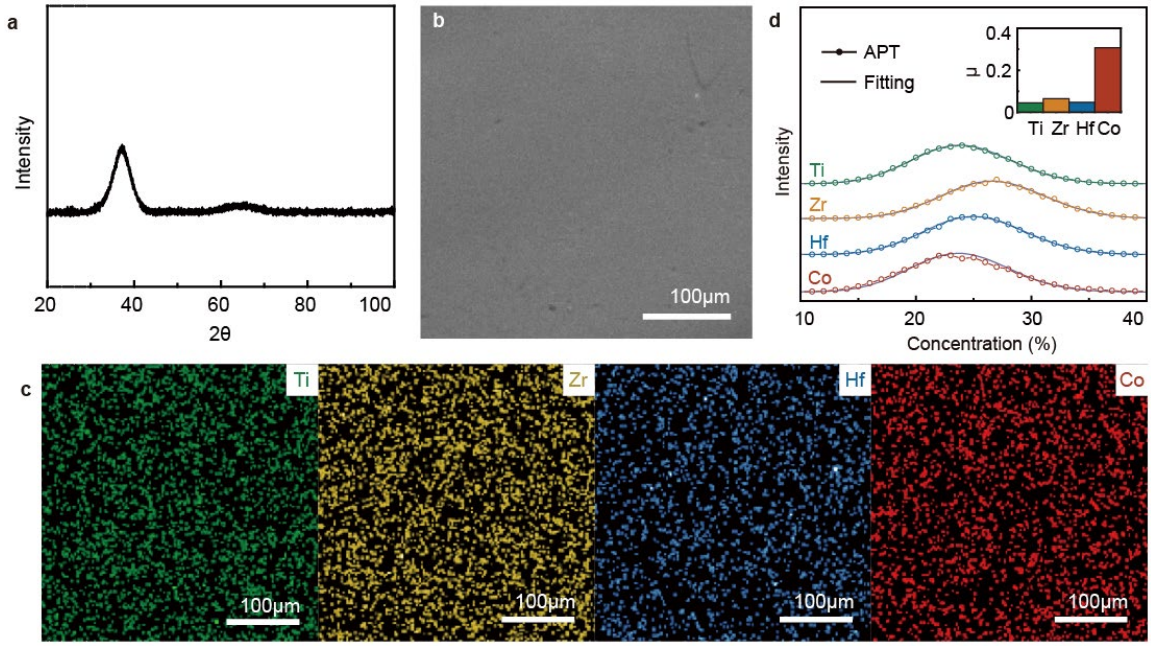

Fig. S1. Structural and chemical characterization of $Ti_{25}Zr_{25}Hf_{25}Co_{25}$ ribbon. a, The XRD pattern shows the amorphous nature of $Ti_{25}Zr_{25}Hf_{25}Co_{25}$ ribbon. The SEM (b) and the corresponding SEM-EDS (c) images show the chemical distribution in the ribbon at the micro-scale. d, The statistical binomial frequency distribution of components. The inset shows the Pearson coefficients (μ).

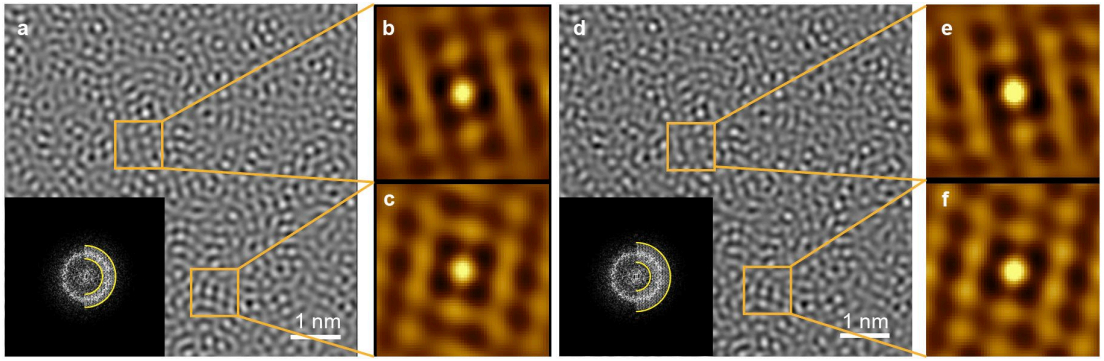

Fig. S2. a and d, the FFT-filtered image of the area selected from Figure 1a (The insets show FFT image of area selected from Figure 1a (left) and the applied filter (right). The yellow curves indicate filters boundary). b, c, e and f, The autocorrelation analysis of local regions.

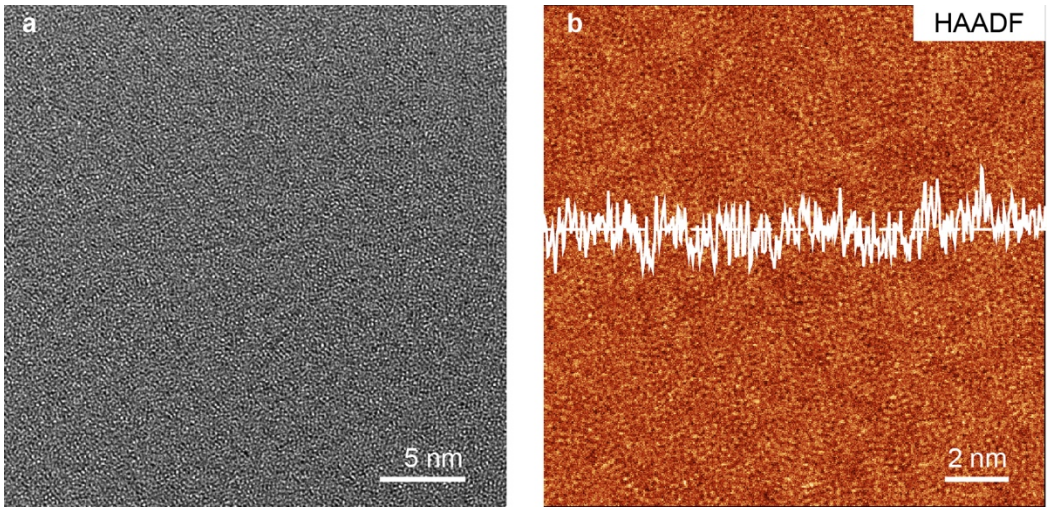

Fig. S3. Structural and chemical characterization of $Zr_{55}Cu_{30}Ni_5Al_{10}$ metallic glass. a, HRTEM image. b, HAADF image.

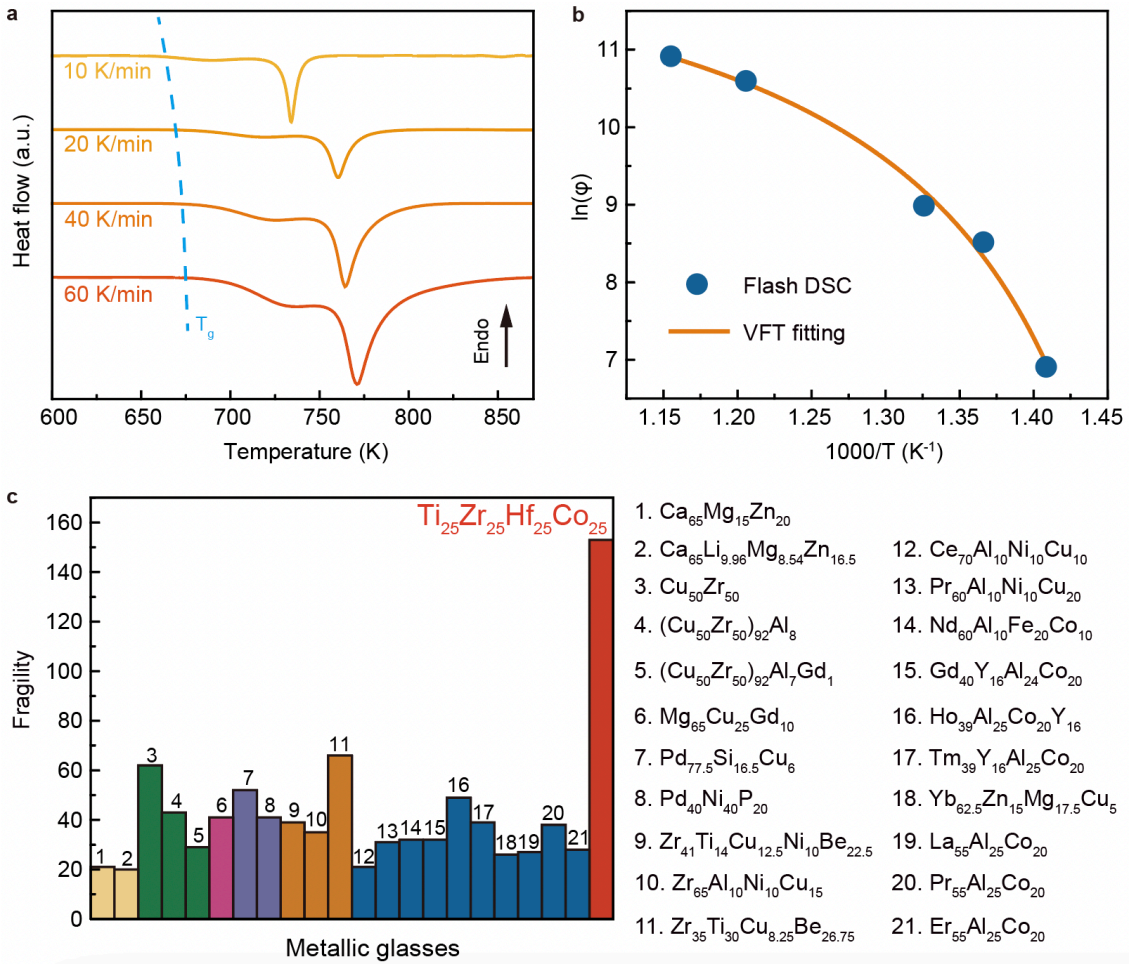

Fig. S4. Thermal analysis of $Ti_{25}Zr_{25}Hf_{25}Co_{25}$ ribbon. a, The conventional DSC heat flow curves of the as-spun samples obtained at the heating rate varying between 10K/min and 60K/min. The dashed line shows the values of T_g extrapolated from the VFT fitting. b, The VFT fitting of T_g of $Ti_{25}Zr_{25}Hf_{25}Co_{25}$ obtained from flash DSC. c, The plot of fragility of $Ti_{25}Zr_{25}Hf_{25}Co_{25}$ in comparison with other metallic glasses(19, 20).

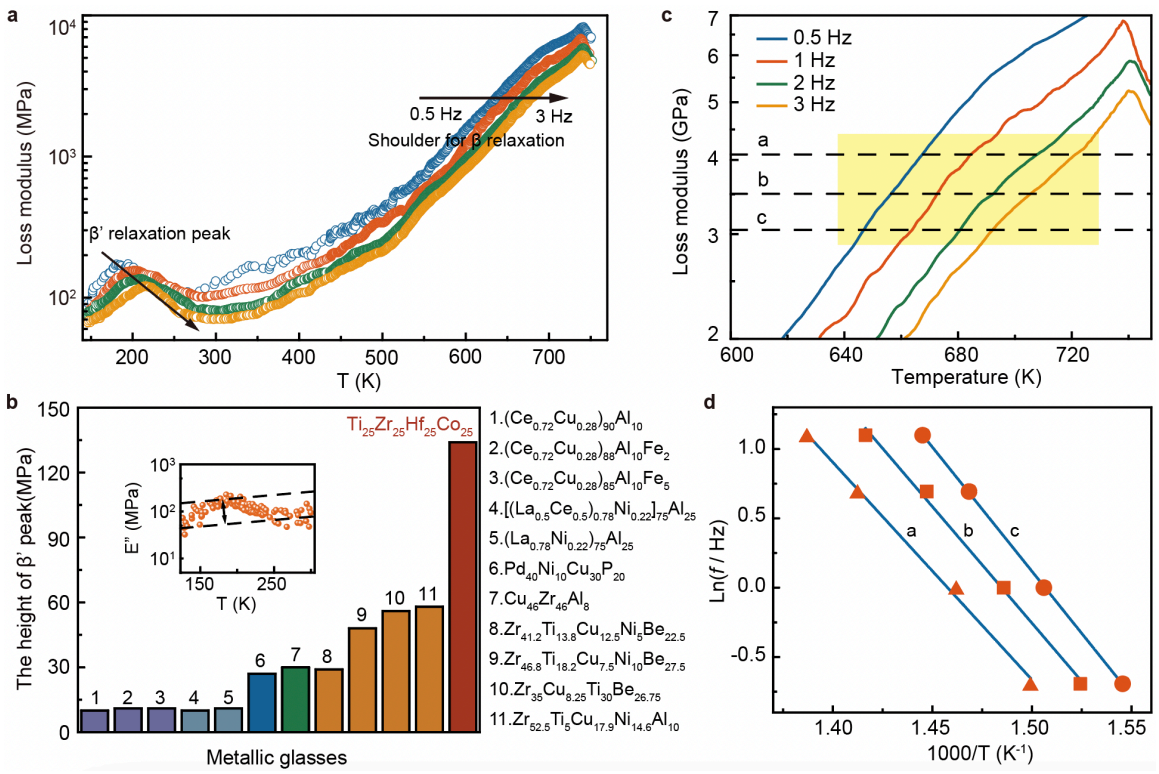

Fig. S5. Dynamic mechanical analysis of $Ti_{25}Zr_{25}Hf_{25}Co_{25}$ ribbon. a, The temperature dependence of storage modulus, E' and loss modulus, E" at the driven frequency of 0.5Hz, 1Hz, 2Hz and 3Hz. b, Comparison of the fast secondary (β') relaxation in metallic glasses in terms of the measured height of the fast secondary relaxation peak (21). The inset shows the enlarged view of the β' relaxation process at 0.5Hz. c, A close view of the E"-T curve near the slow secondary (β) relaxation. Three horizontal dash lines are drawn (line a, b and c) to probe the β relaxation peak. d, The Arrhenius plots for the intersection points defined in c. The slope of the fitted line is -15.7 (line a), -16.8 (line b), -17.9 (line c).

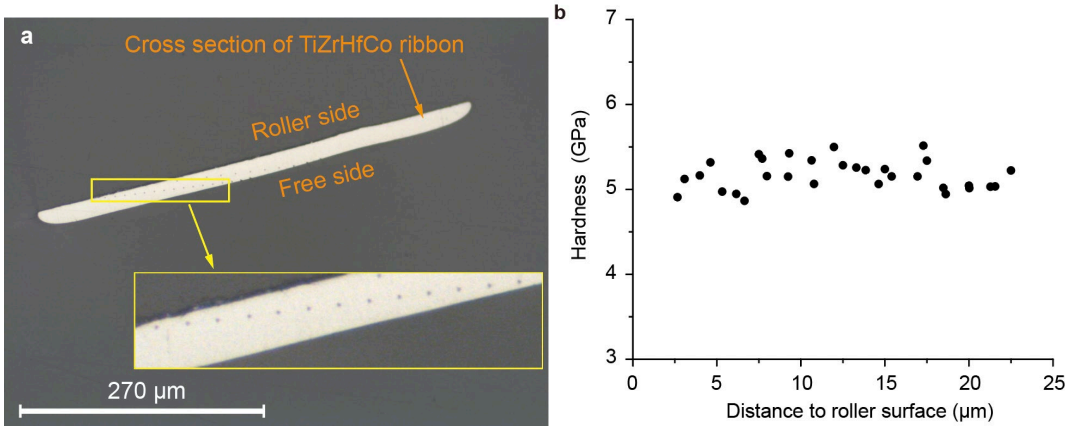

Fig. S6. a. Schematics and indents of Micro indentation tests, b. The hardness along thickness direction.

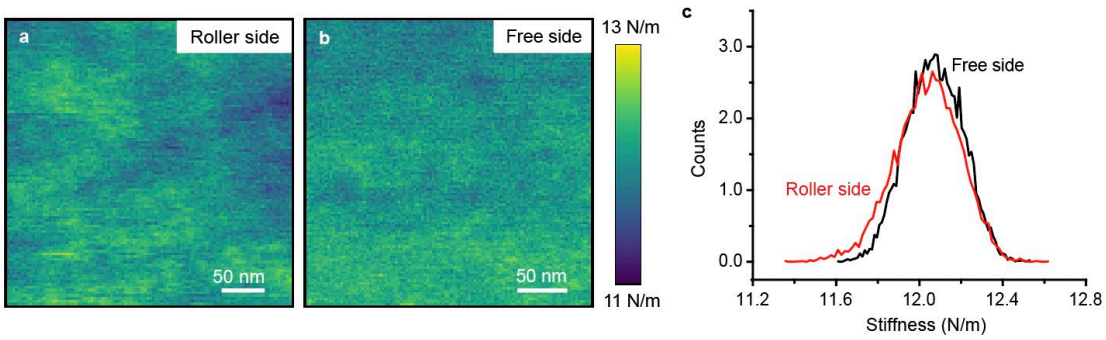

Fig. S7. a and b. The stiffness mapping on the surfaces in contact with and away from the roller, c. The distribution of the nano-scale stiffness on both surfaces.

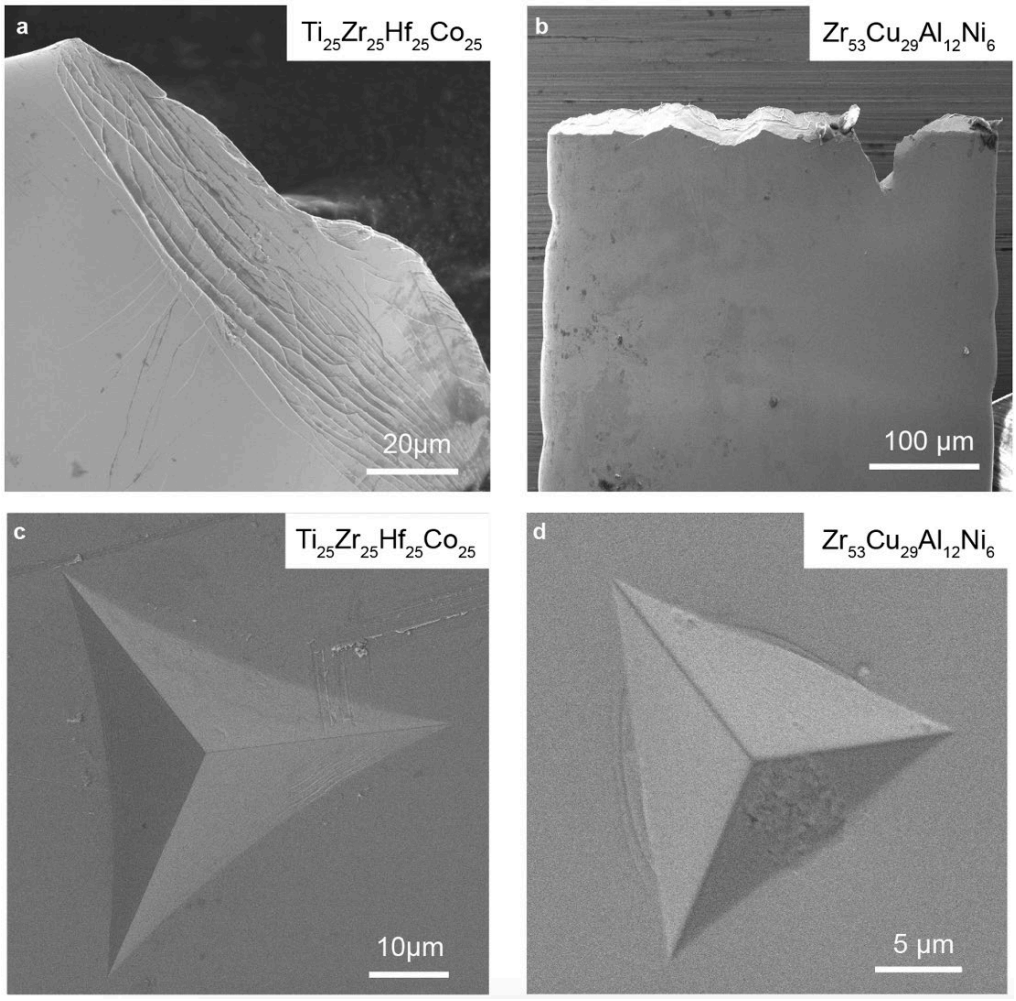

Fig. S8. Mechanical analysis of $Ti_{25}Zr_{25}Hf_{25}Co_{25}$ ribbon. a and b, The top view of the fracture end of $Ti_{25}Zr_{25}Hf_{25}Co_{25}$ and $Zr_{53}Cu_{29}Al_{12}Ni_6$ ribbons, respectively. c and d, SEM images of indentations of $Ti_{25}Zr_{25}Hf_{25}Co_{25}$ and $Zr_{53}Cu_{29}Al_{12}Ni_6$, respectively.

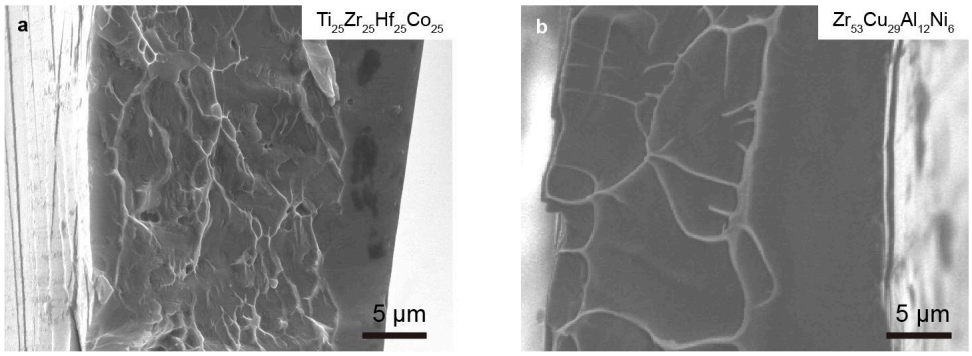

Fig. S9. SEM images of the fracture surfaces of $Ti_{25}Zr_{25}Hf_{25}Co_{25}$ (a) and $Zr_{53}Cu_{29}Al_{12}Ni_6$ (b) after the tensile test.

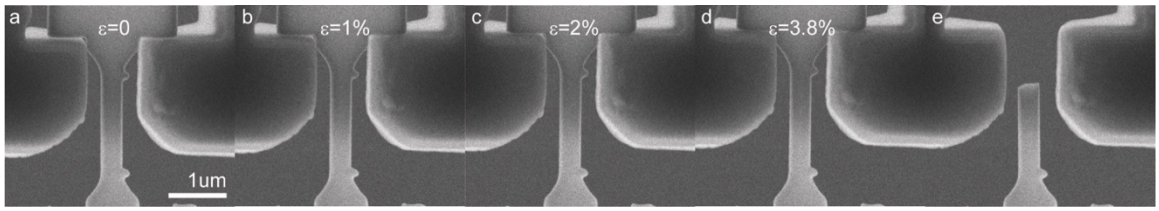

Fig. S10. Images captured during in situ tensile test. The tensile strain is 0 (a), 1% (b), 2% (c), 3.8% (d) and the final fracture (e).

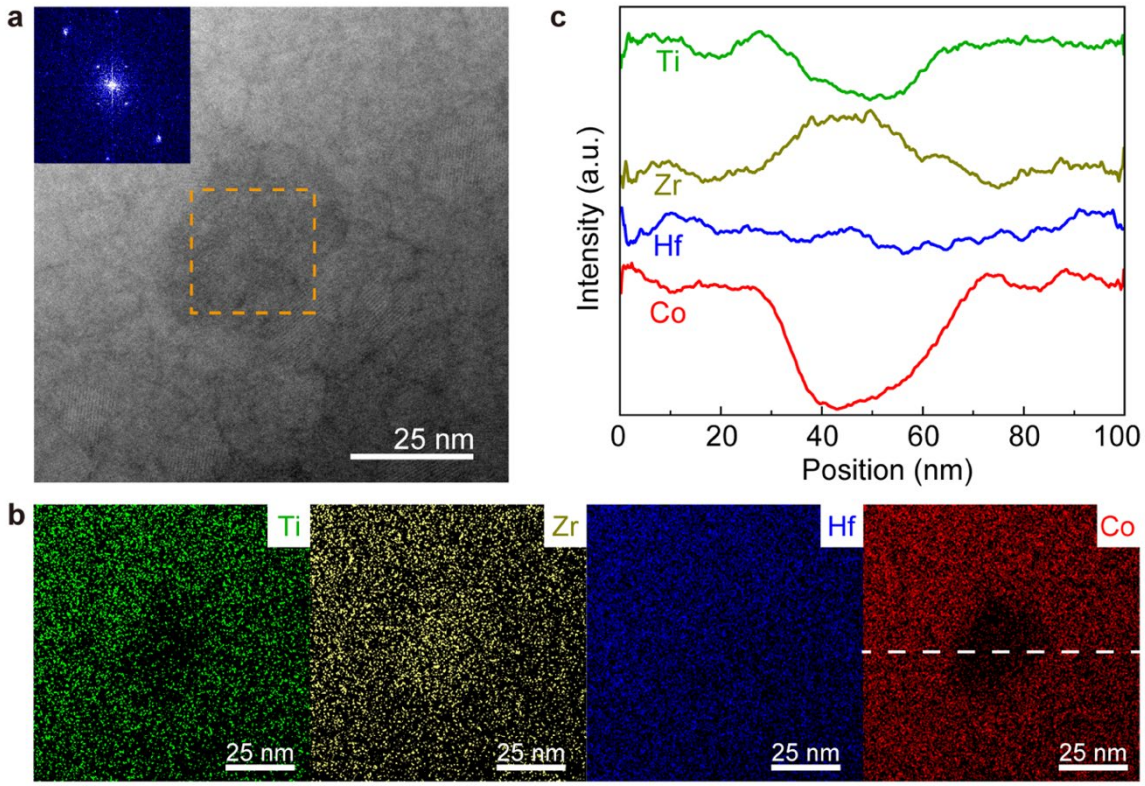

Fig. S11. Structural and chemical characterization of annealed $Ti_{25}Zr_{25}Hf_{25}Co_{25}$ ribbon. a, the HAADF of annealed $Ti_{25}Zr_{25}Hf_{25}Co_{25}$ ribbon. The inset shows FFT pattern of marked region. b, The elemental mapping obtained by STEM-EDS. c, The elemental intensity profiles along the dash line in b.

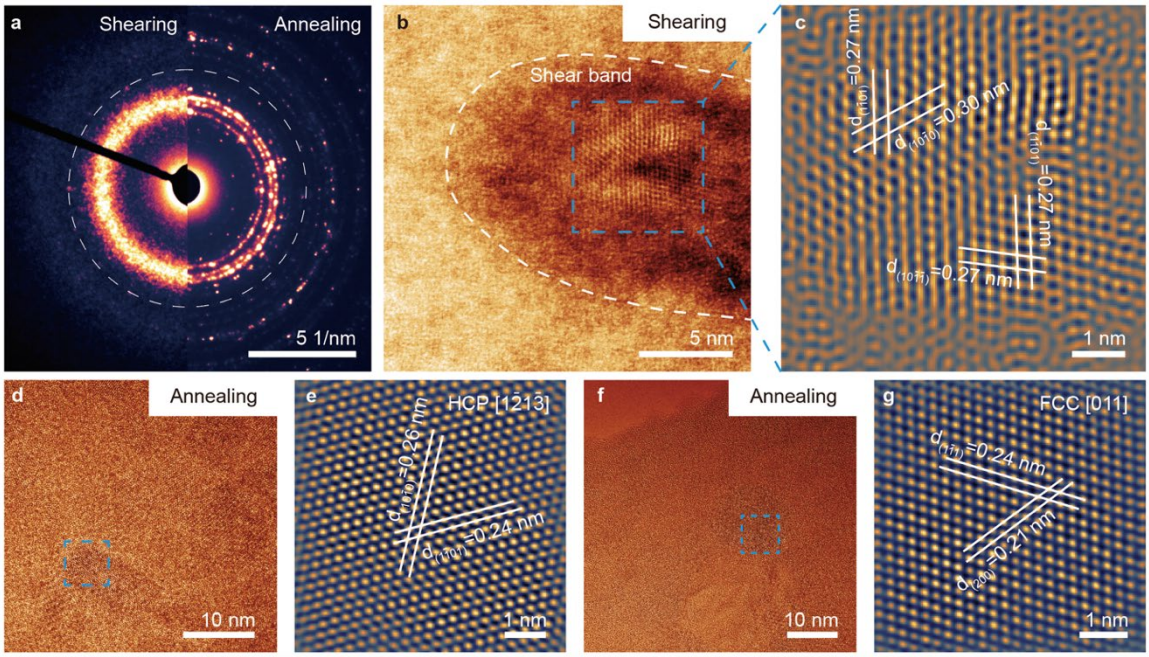

Fig. S12. Structural characterization of shear bands and annealed Ti25Zr25Hf25Co25. a, The comparison of SAED patterns of shear band and annealed Ti25Zr25Hf25Co25, respectively. b, The HAADF image of shear band. c, The IFFT image of local region marked in b. d and f, The HAADF and HRTEM images of annealed Ti25Zr25Hf25Co25, respectively. e and g, The IFFT images of area marked in d and f, respectively.

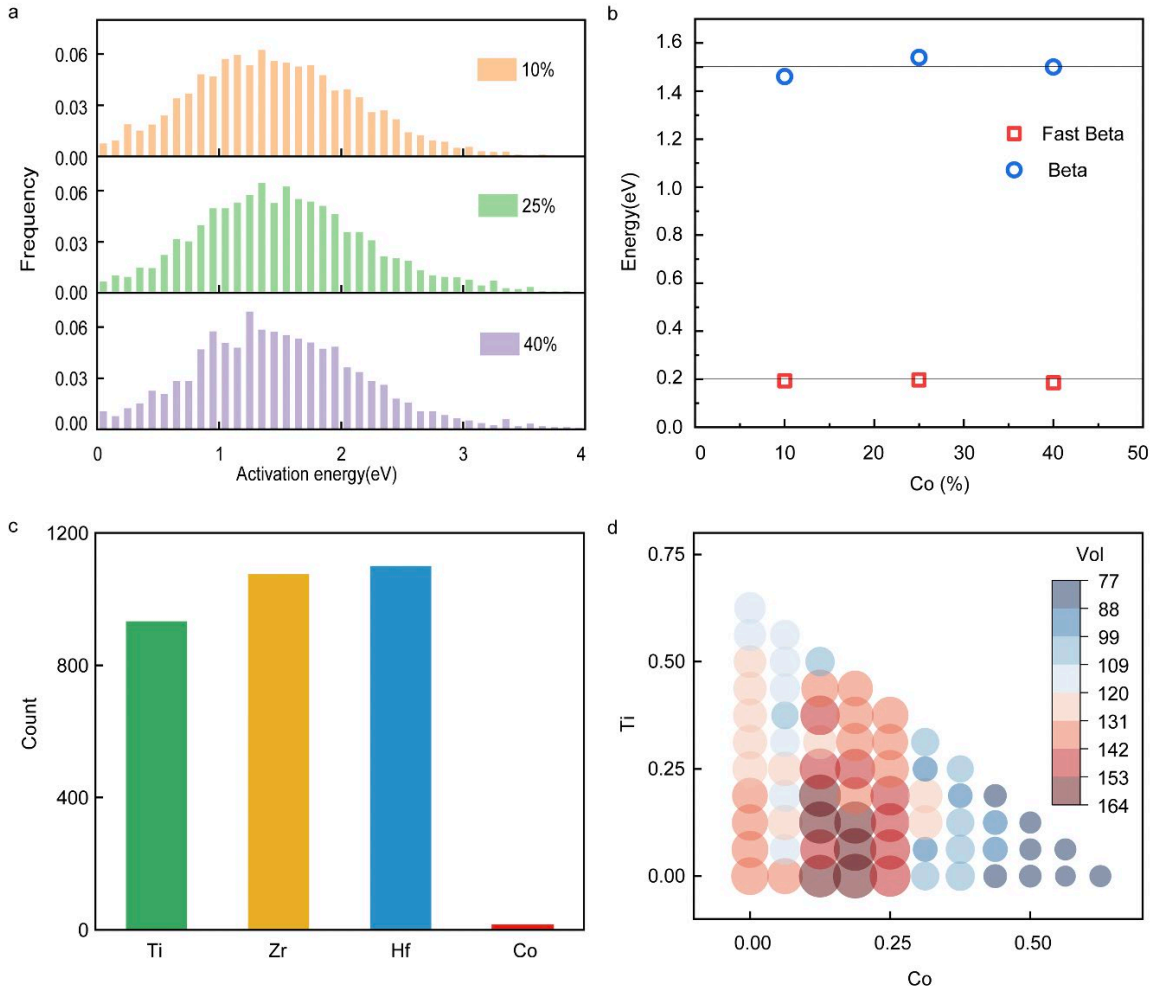

Fig. S13. a, The activation energy distribution and b, The average activation energy for the fast and secondary relaxation processes of the sample with Co concentrations ranging from 6% to 40%. c, Elemental statistics of crystal regions. d, The relationship between the composition and volume of HCP crystals. Based on the results of in Fig. S11, the content of Hf remained almost the same, Zr increased, Ti, and Co decreased. We use 2 degrees of freedom to represent the components of the sample)

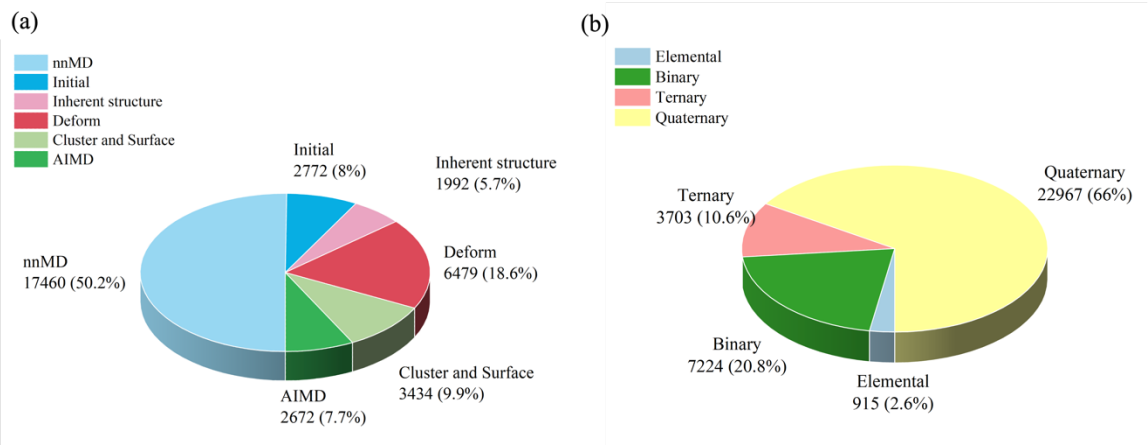

Fig. S14. Compositions of DFT training dataset for the TiZrHfCo MPEMG. Pie chart of the dataset showing (a) the generating methods and (b) the chemical concentrations. AIMD: Ab-initio Molecular Dynamics, and nnMD: neutral network molecular dynamics.

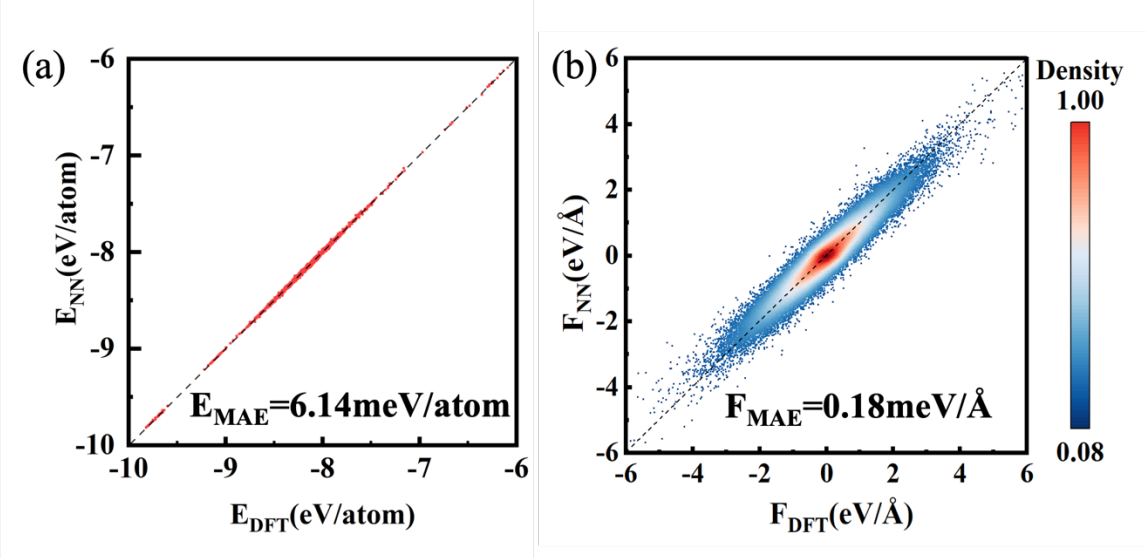

Fig. S15. Calculated energies (a) and force components (b) fitting errors on the testing set. The line of y = x is shown as dashed lines. Data points in (b) are colored by their local number densities. The mean absolute error (MAE) of calculated energies and force components fitting errors on the testing set were 6.14 meV/atom, and 0.18 meV/Å, respectively.

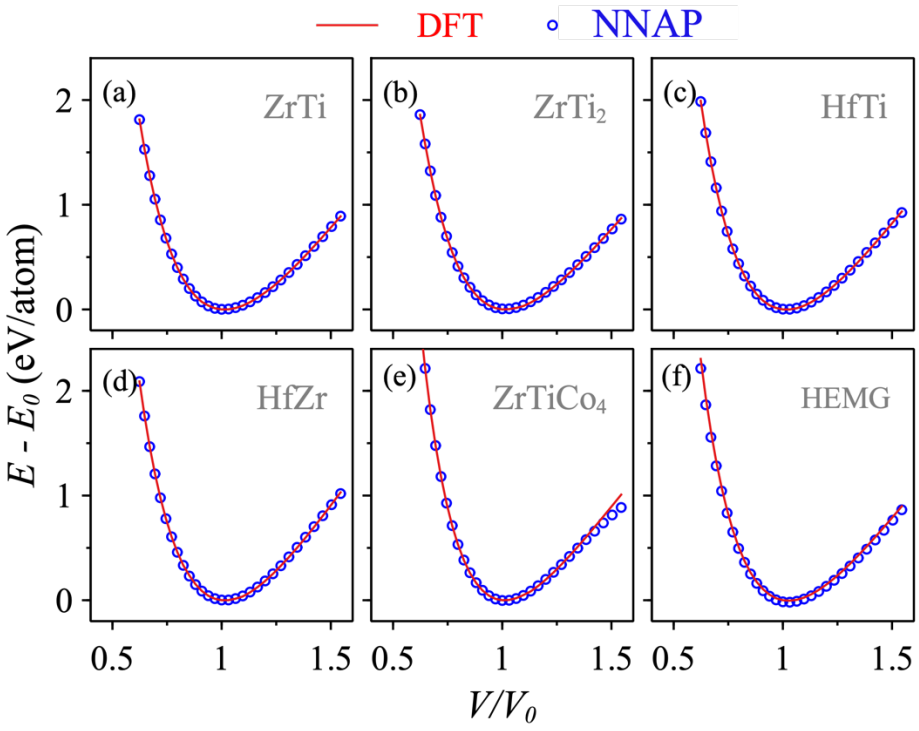

Fig. S16. EOS Validation. Energy per atom as a function of the primitive cell volume for comparison of the DFT benchmark (solid lines) with the NNAP predictions (symbols). (a-e) were crystal, (f) was MPEMG of $Ti_{25}Zr_{25}Hf_{25}Co_{25}$

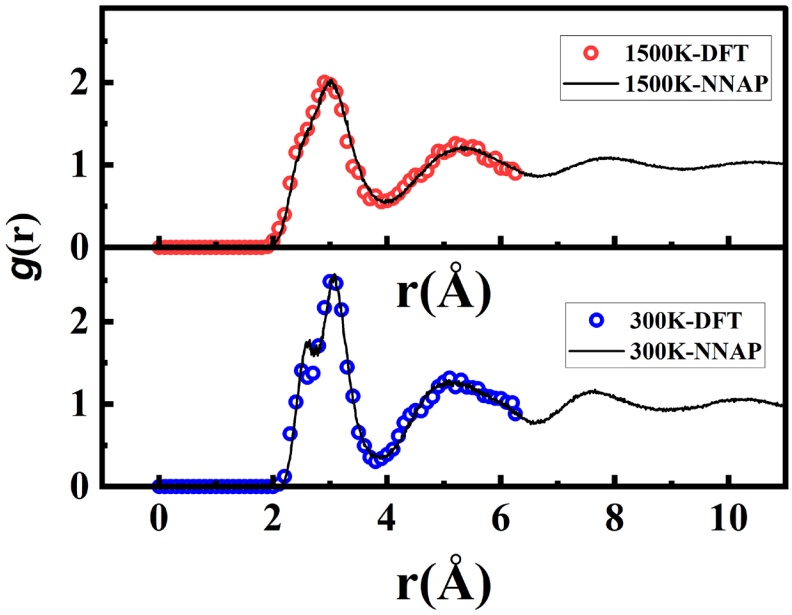

Fig. S17. a and d, the FFT-filtered image of the area selected from Figure 1a (The insets show FFT image of area selected from Figure 1a (left)

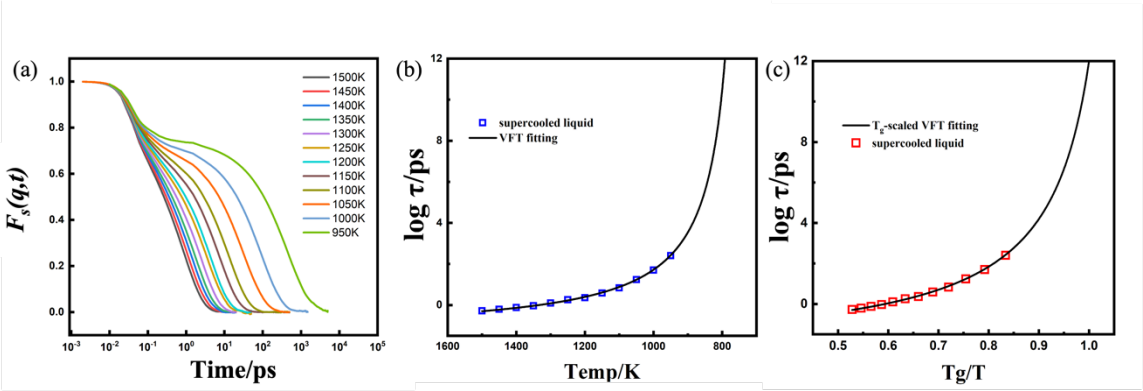

Fig. S18. Thermodynamic property. a, The self-intermediate scattering function curve for different temperatures of $Ti_{25}Zr_{25}Hf_{25}Co_{25}$ MPEMGs. b, The relaxation time $\boldsymbol{\tau_\alpha}$ dependent on temperature T. The solid lines were the VFT function fitting. c, The Angell plot of relaxation time $\boldsymbol{\tau_\alpha}$ versus $\boldsymbol{T_g/T}$ for various systems. The solid lines were the T_g/T-scaled VFT function fitting.

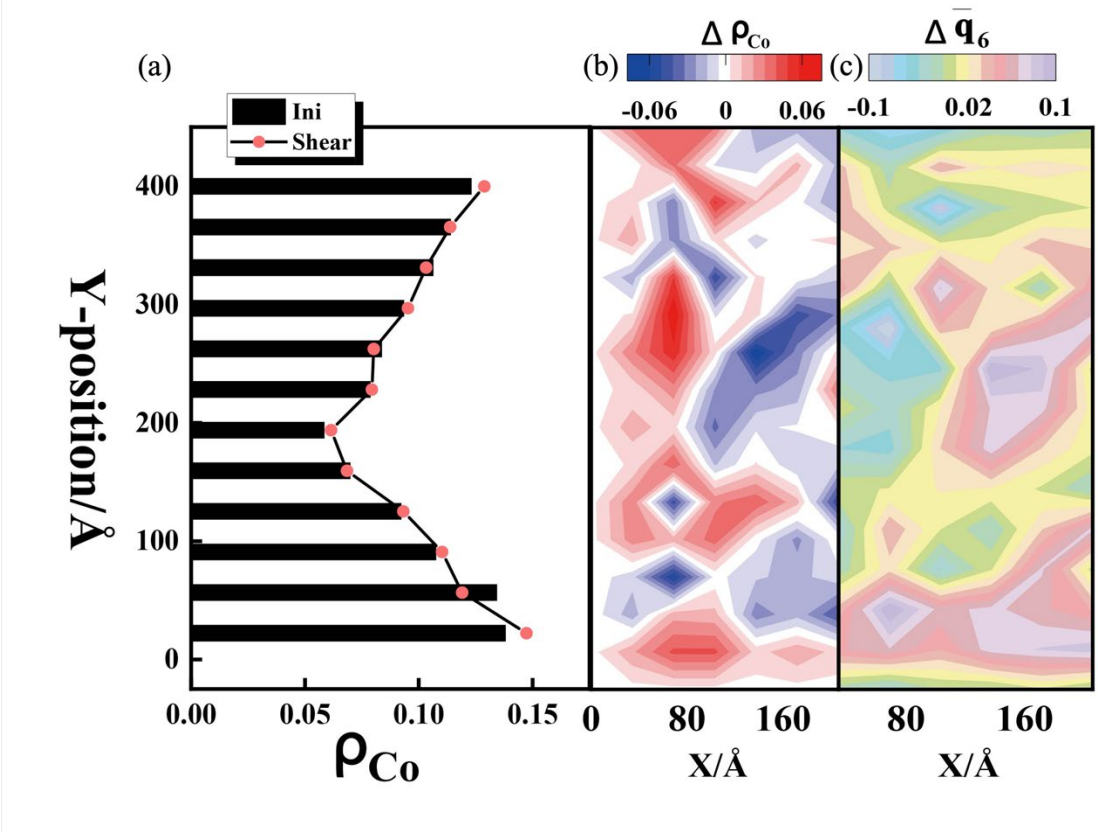

Fig. S19. a, The Co-content of the MD simulated sample in the Y direction before (initial, black bar) and after (red circles) shearing. Spatial distribution contour plot of changes in (b) Co-content and (c) local bond order parameters(17, 22) $\bar{q}_6$ before and after shearing.

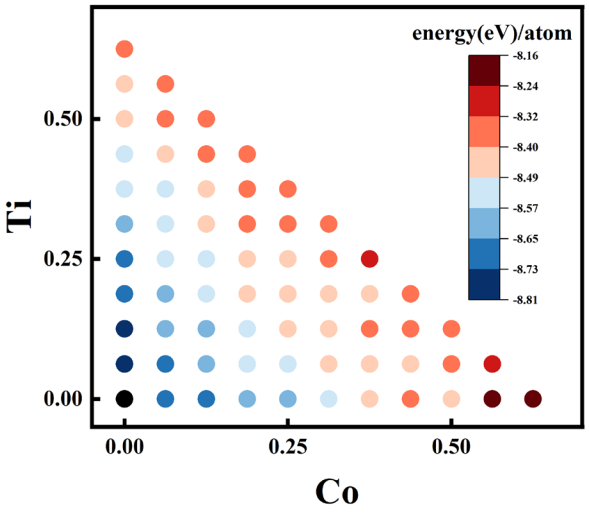

Fig. S20. The relationship between the composition and energy of HCP crystals in Fig. S13d.

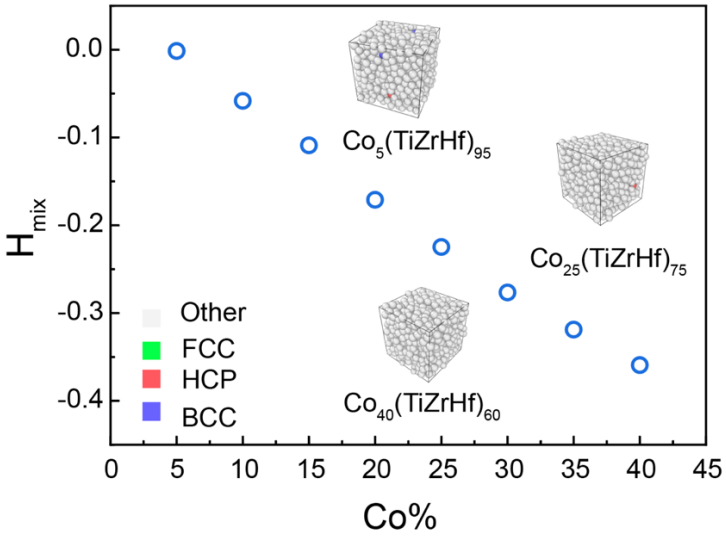

Fig. S21. The relationship between the Co concentration and the calculated enthalpy of mixing between Co and TiZrHf in the $Co_x(TiZrHf)_{1-x}$ system. The insets illustrate the atomic models of $Co_5(TiZrHf)_{95}$, $Co_{25}(TiZrHf)_{75}$, and $Co_{40}(TiZrHf)_{60}$. The color code represents the local packing symmetry based on the neighbor analysis.

Table S1. The fracture strength versus tensile ductility of metallic glasses obtained under uniaxial tensile loading.

	Processing	Fracture strength (GPa)	Tensile ductility (%)	Ref
$Zr_{50}Cu_{30}Ni_{10}Al_{10}$	As cast	1.82	0.03	(23)
$Zr_{64.13}Cu_{15.75}Ni_{10.12}Al_{10}$	As cast	1.68	0.02	(24)
$Cu_{47.5}Zr_{47.5}Al_5$	As cast	1.6	0	(25)
$Zr_{50}M_{50}$ (M=Fe,Co,Ni,Cu)	As cast	1.2	0.23	(26)
$Zr_{64.13}Cu_{15.75}Ni_{10.12}Al_{10}$	Rejuvenating	1.61	0.68	(27)
$Zr_{64.13}Cu_{15.75}Ni_{10.12}Al_{10}$	Rejuvenating	1.67	0.9	(24)
$Zr_{64.13}Cu_{15.75}Ni_{10.12}Al_{10}$	Cold rolling	1.75	0.27	(28)
$Zr_{50}Cu_{30}Ni_{10}Al_{10}$	Cold rolling	1.7	0.5	(29)
$Zr_{52.5}Ti_5Cu_{18}Ni_{14.5}Al_{10}$	Cold rolling	1.8	0.8	(30)
$Cu_{47.5}Zr_{47.5}Al_5$	Cold rolling	1.6	0.7	(25)
$Zr_{65}Fe_5Al_{10}Cu_2$	Surface pattering	1.55	0.72	(31)

Table S2. The calculated mechanical property of $Ti_{25}Zr_{25}Hf_{25}Co_{25}$from experiments (Exp.) and MD simulation (Sim.) with NNAP.

	Exp.	Sim.
Shear Modulus (GPa)	27.7	26.6 （-1.1）
Young's modulus (Gpa)	80	74.5（-5.5）
Poisson Ratio	0.44	0.39（-0.5）

Table S3. The calculated mechanical property parameters with Co concentration MPEMG ranging from 10% to 40% from NN potential (ANN)

	10%Co	25%Co	40%Co
Shear Modulus (GPa)	23.1	26.6	30.4
Young's modulus (Gpa)	64.2	74.5	83.9
Poisson Ratio	0.39	0.4	0.38

Movie S1 (separate file). The regular tensile test of $Ti_{25}Zr_{25}Hf_{25}Co_{25}$ ribbon.

Movie S2 (separate file). The regular tensile test of $Zr_{53}Cu_{29}Al_{12}Ni_6$ ribbon.

Movie S3 (separate file). Diffusion of Co during shearing.

SI References

1. R. Su, J. Yu, P. Guan, W. Wang, Efficient and accurate simulation of vitrification in multi-component metallic liquids with neural-network potentials. 1–32.
2. J. Behler, M. Parrinello, Generalized neural-network representation of high-dimensional potential-energy surfaces. *Phys. Rev. Lett.* **98**, 1–4 (2007).
3. A. P. Bartók, R. Kondor, G. Csányi, On representing chemical environments. *Phys. Rev. B* **87**, 184115 (2013).
4. M. Gastegger, L. Schwiedrzik, M. Bittermann, F. Berzsenyi, P. Marquetand, wACSF—Weighted atom-centered symmetry functions as descriptors in machine learning potentials. *J. Chem. Phys.* **148**, 241709 (2018).
5. C. Zhu, R. H. Byrd, P. Lu, J. Nocedal, Algorithm 778: L-BFGS-B: Fortran Subroutines for Large-Scale Bound-Constrained Optimization. *ACM Trans. Math. Softw.* **23**, 550–560 (1997).
6. F. Birch, Finite Elastic Strain of Cubic Crystals. *Phys. Rev.* **71**, 809–824 (1947).
7. L. Larini, A. Ottochian, C. De Michele, D. Leporini, Universal scaling between structural relaxation and vibrational dynamics inglass-forming liquids and polymers. *Nat. Phys.* **4**, 42–45 (2008).
8. J. Rault, Origin of the Vogel ± Fulcher ± Tammann law in glass-forming materials : the a ± b bifurcation. **271** (2000).
9. S. Zhang, W. Wang, P. Guan, Dynamic Crossover in Metallic Glass Nanoparticles. *Chinese Phys. Lett.* **38** (2021).
10. C. A. Angell, Formation of glasses from liquids and biopolymers. *Science (80-.).* **267**, 1924–1935 (1995).
11. L. Wang, P. Guan, W. H. Wang, The correlation between fragility, density, and atomic interaction in glass-forming liquids. *J. Chem. Phys.* **145** (2016).
12. N. Mousseau, *mfl.*, The Activation-Relaxation Technique: ART Nouveau and Kinetic ART. *J. At. Mol. Opt. Phys.* **2012**, 1–14 (2012).
13. S. Zhang, C. Liu, Y. Fan, Y. Yang, P. Guan, Soft-Mode Parameter as an Indicator for the Activation Energy Spectra in Metallic Glass. *J. Phys. Chem. Lett.* **11**, 2781–2787 (2020).
14. T. Iwashita, T. Egami, Y. Fan, Energy landscape-driven non-equilibrium evolution of inherent structure in disordered material. *Nat. Commun.* **8**, 1–7 (2017).
15. Y.-B. Yang, *mfl.*, Unraveling strongly entropic effect on β-relaxation in metallic glass: Insights from enhanced atomistic samplings over experimentally relevant timescales. *Phys. Rev. B* **102**, 174103 (2020).
16. H. Tanaka, H. Tong, R. Shi, J. Russo, Revealing key structural features hidden in liquids and glasses. *Nat. Rev. Phys.* https:/doi.org/10.1038/s42254-019-0053-3.
17. W. Lechner, C. Dellago, Accurate determination of crystal structures based on averaged local bond order parameters. *J. Chem. Phys.* **129** (2008).
18. X. Luo, *mfl.*, Mixing effect in Zr–Cu metallic liquids. *Model. Simul. Mater. Sci. Eng.* **30**, 85011 (2022).
19. Q. Yang, J. Huang, X. H. Qin, F. X. Ge, H. Bin Yu, Revealing hidden supercooled liquid states in Al-based metallic glasses by ultrafast scanning calorimetry: Approaching theoretical ceiling of liquid fragility. *Sci. China Mater.* **63**, 157–164 (2020).
20. W. H. Wang, The elastic properties, elastic models and elastic perspectives of metallic glasses. *Prog. Mater. Sci.* **57**, 487–656 (2012).
21. Q. Wang, *mfl.*, Universal secondary relaxation and unusual brittle-to-ductile transition in metallic glasses. *Mater. Today* **20**, 293–300 (2017).

22. W. Mickel, S. C. Kapfer, G. E. Schröder-Turk, K. Mecke, Shortcomings of the bond orientational order parameters for the analysis of disordered particulate matter. *J. Chem. Phys.* **138**, 44501 (2013).
23. Y. Yokoyama, K. Inoue, K. Fukaura, Cold-rolled Zr50Cu30Ni10Al10 bulk amorphous alloys with tensile plastic elongation at room temperature. *Mater. Trans.* **43**, 3199–3205 (2002).
24. W. H. Zhou, N. T. Panagiotopoulos, A. L. Greer, Y. Li, Strain-hardening under uniaxial tension in a rejuvenated bulk metallic glass. *Scr. Mater.* **212**, 1–5 (2022).
25. K. K. Song, *mfl.*, Significant tensile ductility induced by cold rolling in Cu 47.5Zr47.5Al5 bulk metallic glass. *Intermetallics* **19**, 1394–1398 (2011).
26. J. Ding, *mfl.*, Novel heating- and deformation-induced phase transitions and mechanical properties for multicomponent Zr50M50, Zr50(M,Ag)50 and Zr50(M,Pd)50 (M = Fe,Co,Ni,Cu) amorphous alloys. *J. Mater. Sci. Technol.* **104**, 109–118 (2022).
27. J. Pan, Y. P. Ivanov, W. H. Zhou, Y. Li, A. L. Greer, Strain-hardening and suppression of shear-banding in rejuvenated bulk metallic glass. *Nature* **578**, 559–562 (2020).
28. Q. P. Cao, *mfl.*, Effect of pre-existing shear bands on the tensile mechanical properties of a bulk metallic glass. *Acta Mater.* **58**, 1276–1292 (2010).
29. Y. Yokoyama, T. Yamasaki, A. Inoue, Significant tensile plasticity of cold rolled Zr50 Cu30Ni10Al10 bulk glassy alloys. *Rev. Adv. Mater. Sci.* **18**, 131–136 (2008).
30. S. Scudino, B. Jerliu, K. B. Surreddi, U. Kühn, J. Eckert, Effect of cold rolling on compressive and tensile mechanical properties of Zr52.5Ti5Cu18Ni14.5Al10 bulk metallic glass. *J. Alloys Compd.* **509**, S128–S130 (2011).
31. R. T. Qu, Q. S. Zhang, Z. F. Zhang, Achieving macroscopic tensile plasticity of monolithic bulk metallic glass by surface treatment. *Scr. Mater.* **68**, 845–848 (2013).